

Highly Conductive Double-Wall Carbon Nanotube Fibers Produced by Dry-Jet Wet Spinning

Hao-Zike Wang, Xin-Yu Jiao, Zhao-Qing Gao, Peng-Xiang Hou,* Le-Le Xu, Chao Shi, Yan Liang, Yun-Peng Wang, and Chang Liu*

Carbon nanotube fibers (CNTFs) are considered an ideal candidate as next-generation conducting wires due to their high conductivity and low density. However, the orientation and compaction of the nanotubes in a CNTF need to be further improved to achieve even higher conductivity and ampacity. Here the fabrication of double-wall CNTFs (DWCNTFs) is reported by a dry-jet wet spinning method, which significantly improves the orientation and compaction of the carbon nanotubes (CNTs). As a result, the obtained DWCNTFs have a record high electrical conductivity of $1.1 \times 10^7 \text{ S m}^{-1}$ and ampacity of $8.0 \times 10^8 \text{ A m}^{-2}$. The fibers also have a high tensile strength of 1.65 GPa and a toughness of 130.9 MJ m^{-3} , among the highest for wet-spun CNTFs. The DWCNTFs preserve their integrity and conductivity after more than 5000 bending cycles. Theoretical calculations indicate that in a dry-jet wet-spinning process, gravity promotes the orientation of the CNTs along the axial direction of the fiber.

density.^[2,12] As a result, they are regarded as an ideal material for assembling lightweight, highly conductive fibers. However, the excellent properties of CNTs decrease by orders of magnitude when they are assembled to form macroscopic fibers,^[13,14] which greatly limits their practical use.

Among the methods for CNTF preparation,^[13–17] wet spinning from a lyotropic liquid-crystalline solution produces CNTFs with high electrical and thermal conductivities and reasonable mechanical properties.^[18–20] However, both the electrical conductivity and mechanical properties of the obtained CNTFs are much lower than those of the individual CNTs, which is caused by the introduction of contact resistance and weak inter-tube interactions between the CNTs. It was

found that the orientation and compaction of CNTs are two key factors that determine the number and size of inter-tube contacts and this determines the performance of the CNTFs.^[21–23] Therefore, great effort has been devoted to forming dense and highly oriented CNTFs.^[13,14,18–20,24] However, little attention has been paid to cracks in the CNTFs, which originate from the diffusion of the coagulation bath from the shell to the core of a fiber, forming a concentration gradient in the radial direction.^[18] These cracks greatly decrease the CNTF performance due to the introduction of irregular pores.

Dry-jet wet spinning is efficient in improving the orientation of polymer macromolecules and reducing cracks^[25,26] in fibers because of the pre-orientation effect in the air gap.^[27] However, the dry-jet wet-spinning method has not been used for the fabrication of CNTFs. In this work, we fabricated double-wall CNTFs (DWCNTFs) with high conductivity and high ampacity using a dry-jet wet spinning method (**Figure 1**). We found that long DWCNTs with high molecular weight could be successfully spun under a stable and long air gap. The DWCNTs are highly oriented along the fiber axis by gravity and shear forces from the solvent, which reduces the core-shell orientation difference as compared to the fibers obtained by common wet spinning.^[28] The obtained DWCNTFs have a high degree of orientation (Herman factor) of 0.994 and a high compaction density of 1.96 g cm^{-3} . As a result, the DWCNTFs showed not only a record high electrical conductivity of $1.1 \times 10^7 \text{ S m}^{-1}$ and ampacity of $8.01 \times 10^8 \text{ A m}^{-2}$, but also a high tensile strength of 1.65 GPa and

1. Introduction

High-performance fibers with high electrical conductivity, high strength and toughness, low density, and easy manufacture into textiles and composites, are greatly needed to replace conventional Cu^[1,2] in sensors,^[3] aeroengines,^[4] electromagnetic interference shielding,^[5] inverters,^[6] etc. Carbon nanotubes (CNTs) with a 1D tubular structure have excellent physiochemical properties including high ampacity,^[7] high strength,^[8,9] high conductivity,^[10,11] as well as excellent chemical stability and low

H.-Z. Wang, X.-Y. Jiao, Z.-Q. Gao, P.-X. Hou, L.-L. Xu, C. Shi, Y. Liang, C. Liu

Shenyang National Laboratory for Materials Science
Institute of Metal Research
Chinese Academy of Sciences
Shenyang 110016, China
E-mail: pxhou@imr.ac.cn; cliu@imr.ac.cn

H.-Z. Wang, X.-Y. Jiao, P.-X. Hou, L.-L. Xu, C. Liu
School of Materials Science and Engineering
University of Science and Technology of China
Hefei 230026, China

Y.-P. Wang
School of Materials Science and Engineering
Dalian University of Technology
Dalian 116024, China

The ORCID identification number(s) for the author(s) of this article can be found under <https://doi.org/10.1002/adfm.202404538>

DOI: 10.1002/adfm.202404538

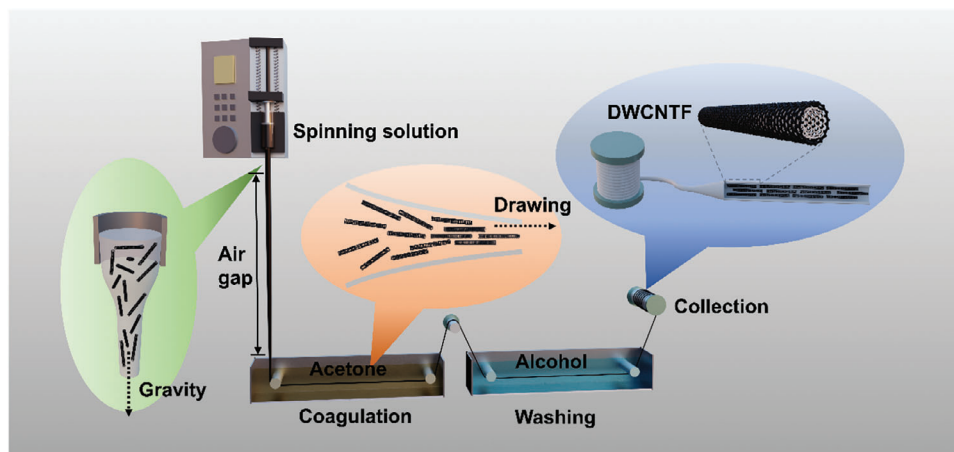


Figure 1. Schematic showing the fabrication of DWCNTFs by the dry-jet wet spinning method.

a high toughness of 130.9 MJ m^{-3} . They also have excellent flexibility and a resistance that is constant over a wide temperature range.

2. Results

2.1. Fabrication of DWCNTFs

DWCNTs with a mean outer diameter of 2.0 nm (Figure S1a, Supporting Information) were synthesized using a floating catalyst chemical vapor deposition (FCCVD)^[29–31] method. The prepared samples are highly pure and well crystalline as characterized by TEM, Raman, and TG analysis (Figure S1b–d, Supporting Information). The DWCNTs were then dispersed in chlorosulfonic acid (CSA)^[32] to form a liquid crystal phase (LC; Figure S2, Supporting Information), and the critical DWCNT concentration for forming the LC is 0.08 wt\% . We measured the lengths of 100 DWCNTs based on scanning electron microscopy (SEM) observations (Figure S3a, Supporting Information) and found that $\approx 80\%$ of the nanotubes have lengths ranging from 15 to $35 \text{ }\mu\text{m}$ (Figure S3b, Supporting Information), and the mean tube length is $\approx 24 \text{ }\mu\text{m}$. Therefore, the aspect ratio of the dispersed DWCNTs in the LC is calculated to be $\approx 15\,000$. The high quality of the raw DWCNT material together with this high aspect ratio remaining in the LC would be beneficial to achieve the excellent properties of the fabricated fibers.^[18,20,33]

We designed and constructed a new wet spinning setup, where an air gap was introduced to achieve close packing and good alignment of the DWCNTs with the aid of gravitational forces, as schematically shown in Figure 1. The spinning of the DWCNTFs is shown in Video S1 (Supporting Information). Compared to the previously reported normal wet spinning of CNT fibers, the main difference is that the DWCNT LC passes through an air gap before entering the coagulation bath (Figure S4, Supporting Information), and the obtained fibers are denoted as AG-DWCNTFs. We also fabricated CNT fibers using the normal wet spinning technique without introducing an air gap for comparison, which are denoted as N-DWCNTFs.

2.2. Structure Characterization of DWCNTFs

Figure 2a,b respectively show typical SEM images of the AG-DWCNTFs and N-DWCNTFs. We can see that the diameter of an AG-DWCNTF is much smaller than an N-DWCNTF, and the surface of the former is much smoother. High magnification SEM images (Figure S5, Supporting Information) show that numerous DWCNTs are densely packed and well aligned in the AG-DWCNTF, while many more pores and misaligned tubes are observed in the N-DWCNTF. To further investigate the structural uniformity of the fibers, their cross-sections were examined. Figure 2c,d, shows typical cross-sectional SEM images of AG-DWCNTF and N-DWCNTF cut by a focused ion beam (FIB), respectively. The AG-DWCNTF has a smooth, uniform, and dense cross-section (Figure 2c; Figure S6a, Supporting Information), while several cracks are obvious in the cross-section of the N-DWCNTF (Figure 2d; Figure S6b, Supporting Information). This morphology difference originates from the air gap, where the gravity equally acts on the core and shell of the fiber and promotes the orientation of CNTs while avoiding the formation of the core-shell structure commonly observed in normal wet spun CNT fibers (Figure S7, Supporting Information).^[28,34–36] In addition, the density of the AG-DWCNTF was measured to be 1.96 g cm^{-3} , much higher than that of N-DWCNTF (1.61 g cm^{-3}). The improvement in orientation, compaction, and density is attributed to the introduction of a long air gap during the fabrication of AG-DWCNTFs, where the effect of gravity helps achieve a denser and more perfectly aligned structure.

Wide angle X-ray scattering (WAXS) measurements were performed to evaluate the degree of orientation of the nanotubes in the fiber.^[5,14,19,37] The WAXS patterns (Figure 2e,f) show that AG-DWCNTF has a narrow diffraction range, while that of N-DWCNTF is much wider. The Herman orientation factor of AG-DWCNTF calculated by integration of the azimuth angle of the WAXS pattern^[5,38–40] is 0.994 , which is much higher than 0.942 for N-DWCNTF and close to the highest previously reported value of 0.996 .^[19] These results confirm the improvement in the nanotube orientation using gravity during the dry-jet wet spinning process.

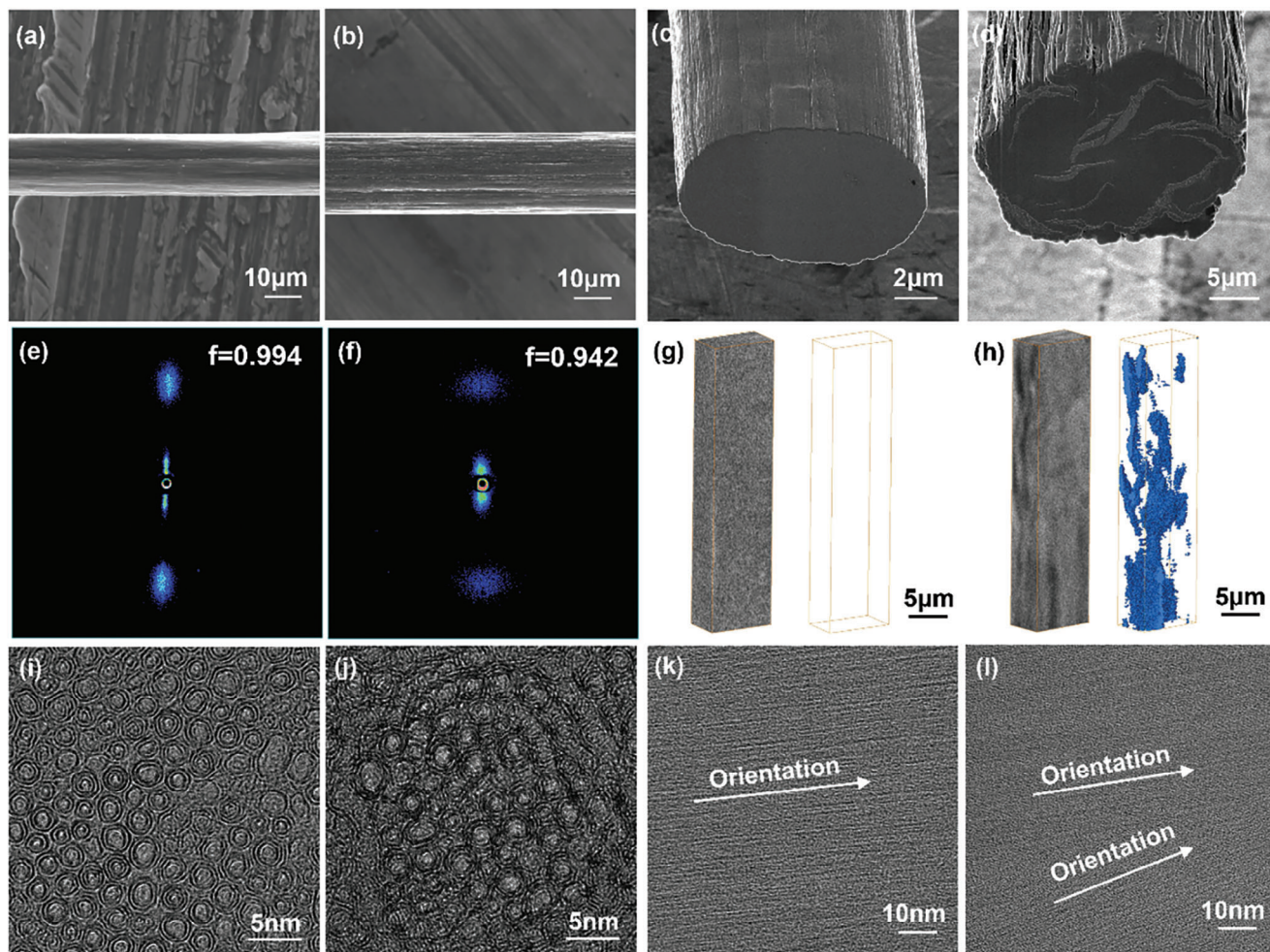


Figure 2. Morphology characterizations of DWCNTFs. SEM images of a) AG-DWCNTF and b) N-DWCNTF. Cross-sectional SEM images of c) AG-DWCNTF and d) N-DWCNTF. WAXS patterns of e) AG-DWCNTF and f) N-DWCNTF. XRM images of g) AG-DWCNTF and h) N-DWCNTF. Cross-sectional TEM images of i) AG-DWCNTF and j) N-DWCNTF. Axial-direction section TEM images of k) AG-DWCNTF and l) N-DWCNTF.

We also performed 3D X-ray microscopy (XRM) measurements with a spatial resolution of 150 nm to investigate the typical internal 3D structure of the fibers. As shown in Figure 2g and Figure S8a (Supporting Information), there are no pores detected in the AG-DWCNTF, while obvious pores are seen inside the N-DWCNTF (Figure 2h; Figure S8b and Video S2, Supporting Information), which is consistent with the SEM observations. The typical cross-sectional structure of the fibers was characterized by using high-resolution transmission electron microscopy (HRTEM), and the TEM sample was prepared by FIB cutting. As shown in Figure 2i and Figure S9a,b (Supporting Information), the CNTs in AG-DWCNTF are densely packed and there are almost no voids observed. It is clearly seen that almost all the tubes are double-walled, confirming the high purity of the DWCNT raw material employed. In contrast, some voids are observed in the N-DWCNTF (Figure 2j; Figure S9c,d, Supporting Information). Cross-sectional HRTEM images in the axial direction of the two samples are shown in Figure 2k,l. As for the AG-DWCNTF (Figure 2k; Figure S10, Supporting Information), the DWCNTs are well-aligned parallel to the axial direction, which

is consistent with the WAXS and SEM observations. However, CNTs are not well aligned in parallel along the axial direction of the N-DWCNTF where an included angle of $\approx 15^\circ$ was observed (Figure 2l).

In order to understand the function of gravity in the air gap on the structure of DWCNTFs, we tuned the air gap lengths as 5, 10, and 15 cm, and used the maximum draw ratio that can be tolerated in subsequent collections of AG-DWCNTFs, and the resulting samples are denoted AG-DWCNTF-5, AG-DWCNTF-10, and AG-DWCNTF-15, respectively. We note that the length of the air gap would affect the final draw ratio (Figure S11, Supporting Information). It is worth noting that when the length of the air gap exceeds 15 cm, the jetting of the DWCNT solution becomes unstable. It was found that the Herman orientation factors of the fabricated fibers increase with increasing air gap length (Figure 3a; Figure S12, Supporting Information). At the same time, the diameters of the fibers decrease while the densities increase with an increased degree of orientation as shown in Figure 3b, Figure S13 and Table S1 (Supporting Information). It is well known that positive traction during spinning leads to the

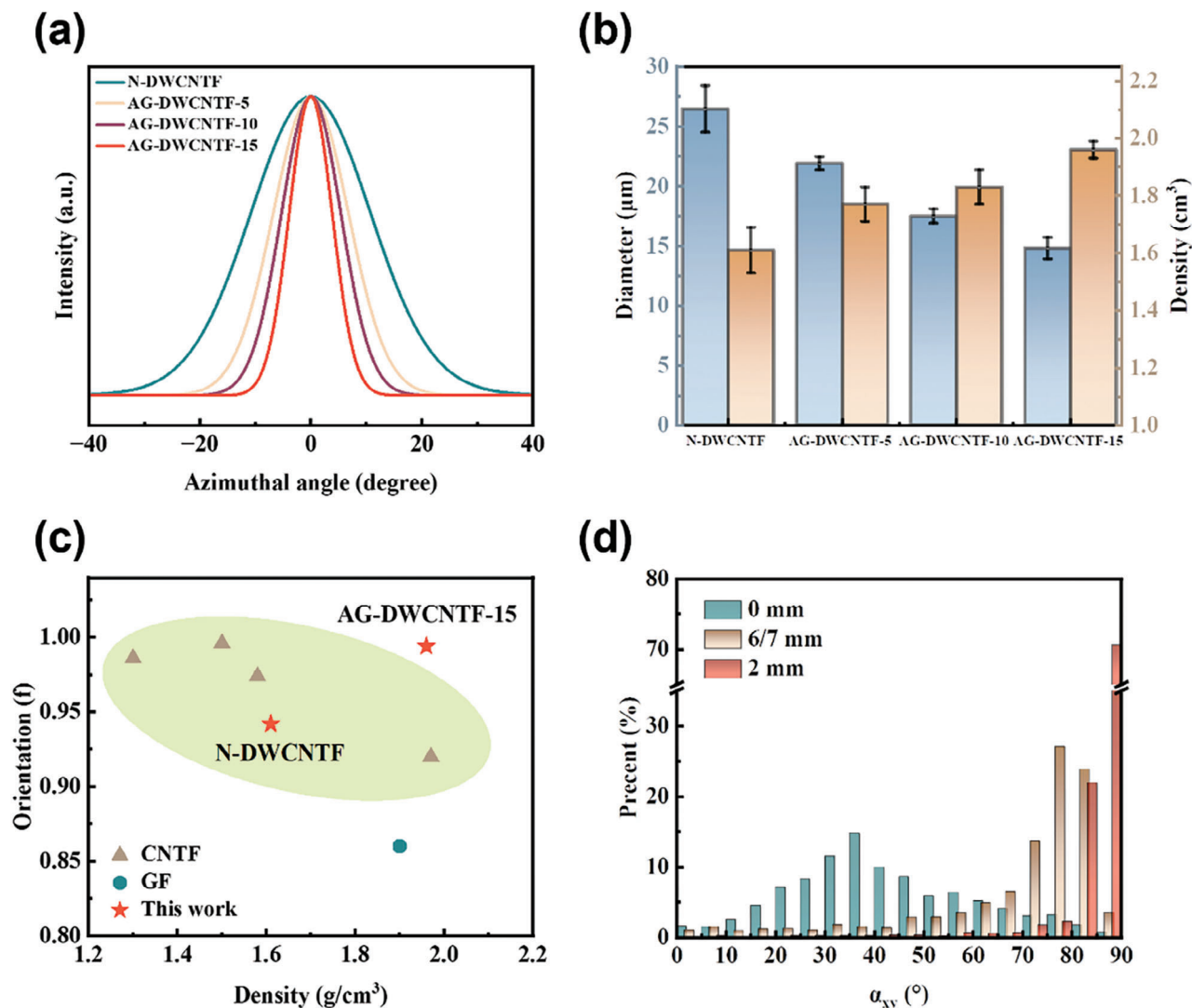


Figure 3. Structure characterization of the DWCNTFs. a) Azimuthal scan curves of different fibers from WAXS patterns. b) Comparison of diameter and density of N-DWCNTF, AG-DWCNTF-5, AG-DWCNTF-10 and AG-DWCNTF-15. c) Comparison of density and orientation of previously reported CNTFs, GF, N-DWCNTFs, and AG-DWCNTF-15. d) Simulated angle distribution of CNTs at 0 mm, 6/7 mm and 2 mm in the air gap.

densification of the spun fibers.^[18,40] In this work, we increased this effect by introducing an air gap to use gravity, and the traction can be easily tuned by changing the length of this gap. As a result, at an optimum condition, the density of AG-DWCNTF-15 was increased by 22% and the Herman orientation factor reached 0.994. We compared the orientation and density of our DWCNTFs with previously reported CNTFs and graphene fiber (GF) in Figure 3c.^[13,20,22,30,32] It can be seen that our sample has the highest Herman orientation factor and the highest density.

By using the discrete element and fluid coupling calculation method, we simulated the motion of 1000 CNTs in the spinning solution under gravity. In order to simplify the calculation, we set the length of the air gap to be less than 2 mm. More details are given in the experimental section. At the beginning of the air gap, the orientation of CNTs is relatively random (Figure S14, Supporting Information). Due to the gravity, the spinning solution gradually shrinks, and the CNTs tend to be vertically aligned.

We define the angle between the CNTs and the vertical as α_{xy} . Figure 3d and Figure S15 (Supporting Information) are the real-time angular distributions of CNTs at different lengths of the air gap, which shows that α_{xy} becomes narrower and approaches 90° with the increasing air gap length. The average α_{xy} is shown in Figure S15f (Supporting Information), and increases from 41.9° to 84.3° , confirming the function of gravity in the orientation of CNTs. The above-simulated result indicates that introducing an air gap to use gravity in a wet-spinning process leads to the alignment of the CNTs with the gravitational force.

2.3. Properties of AG-DWCNTFs

We measured the electrical conductivity of the DWCNTFs and found that it increases with increasing length of the air gap, which is attributed to the increasing orientation and density due

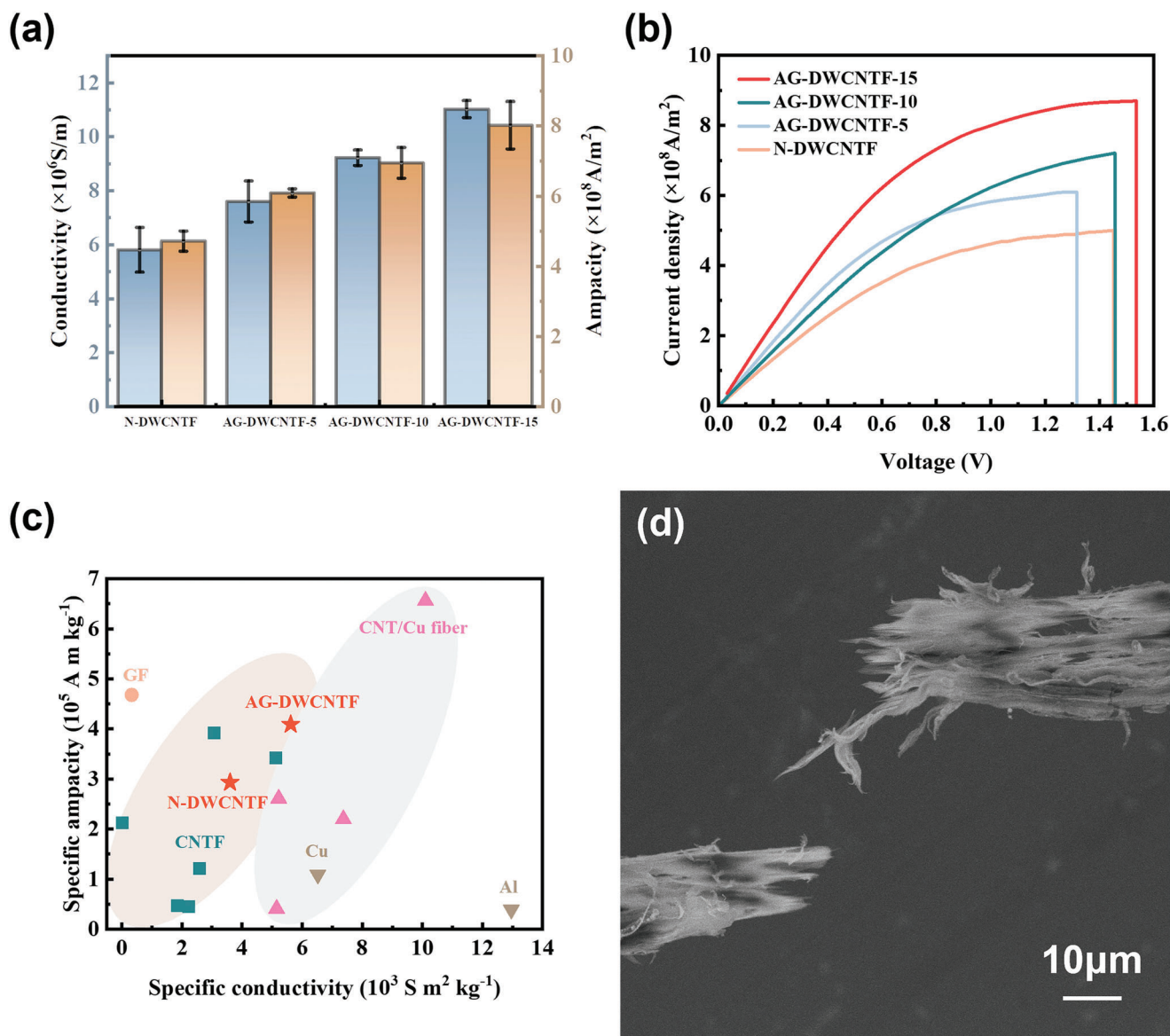


Figure 4. Electrical properties of DWCNTFs. a) The conductivity and ampacity of the DWCNTFs. b) Current density-voltage curves of the DWCNTFs. c) A comparison of specific conductivity and specific ampacity of previously reported CNT fibers, GF, metals, CNT/Cu fibers and our DWCNTFs. d) Typical SEM image of the AG-DWCNTF broken by Joule heating.

to gravity (Figure 4a; Table S2, Supporting Information). AG-DWCNT-15 had a high conductivity of $(11.01 \pm 0.32) \times 10^6 \text{ S m}^{-1}$, which is the highest value reported for CNT fibers. Ampacity is the capacity of the maximum current carried by the conductor before it fails under high currents.^[41] We measured the current passed when gradually increasing the voltage and calculated the ampacity of the fibers. As shown in Figure 4a,b, AG-DWCNTF-15 showed the highest ampacity of $(8.01 \pm 0.68) \times 10^8 \text{ A m}^{-2}$, which is even higher than Al, and similar to Cu.

Considering the low density of the CNTFs, we calculated the specific conductivity and specific ampacity of our fibers. An Ashby plot of specific ampacity versus specific electrical conductivity of previously reported CNTFs, GF, CNT/Cu fibers, our DWCNTFs, and traditional conducting metals is shown in

Figure 4c and Table S3 (Supporting Information).^[1,14,41–48] It can be seen that our AG-DWCNTF has a high specific conductivity of $5.62 \times 10^3 \text{ S m}^2 \text{ kg}^{-1}$, which is close to the reported highest value for CNTFs, and is 86% of the value for Cu. The specific ampacity is $4.09 \times 10^5 \text{ A m kg}^{-1}$, three times that of a commercial Cu wire ($1.09 \times 10^4 \text{ A m kg}^{-1}$). In order to better understand the failure behavior of our DWCNTF under high currents, its structure after failure was characterized by SEM (Figure 4d; Figure S16, Supporting Information). It can be seen that the broken tips are clean, which is characteristic of current-induced Joule heating and consistent with references.^[41,49] As shown in Figure S17 (Supporting Information), the failure temperature is estimated to be $\approx 694^\circ \text{C}$. Therefore, the high current-carrying ability of our DWCNTFs may originate from the rapid local

excessive Joule heat transfer by the highly oriented and compact CNTs.

We also characterized the mechanical properties of our DWCNTFs. As shown in Figure 5a,b and Table S2 (Supporting Information), both the tensile strength and the toughness of the AG-DWCNTF are higher than that of N-DWCNTF due to the introduction of the air gap. Moreover, the strength and toughness of the fibers increase with increasing air gap length. The highest tensile strength and toughness were 1.65 GPa and $\approx 130.9 \text{ MJ m}^{-3}$, respectively. This phenomenon is reasonable when considering the CNTF stretching model,^[50] in which the strength of the fiber is proportional to tube–tube interface contact area ($\Omega_1\Omega_2$), the shear strength between CNTs, and the average length of CNTs. For AG-DWCNTF, CNTs are tightly packed and highly oriented along the fiber axis (Figure S18, Supporting Information), which leads to a larger effective tube–tube interface contact area ($\Omega_1\Omega_2$). Therefore, AG-DWCNTF shows higher toughness and strength than those of N-DWCNTF. The elongation at break of our fibers was as high as 12.42%, which is three times that of previously reported wet-spun fibers^[14,18,20] (Figure S19, Supporting Information). Zhang et al. suggested that the failure mechanism of CNTFs during stretching is a slip between CNTs,^[51] which is characterized by inter-tube slippage at a low strain rate. To understand this better, the fracture planes were studied by SEM. As shown in Figure 5c and Figure S20 (Supporting Information), the fiber splits into multiple ribbons, which is characteristic of pull-out fracture, indicating a sliding-to-break mechanism. This failure mechanism means that the elongation at the break of the fiber is positively correlated with the length of CNTs. As summarized in Figure 5d and Table S3 (Supporting Information), the AG-DWCNTFs have a larger elongation at break and a larger toughness compared with previously reported CNT fibers,^[20,52–55] Kevlar fibers,^[56] GFs^[39,57] and CNT composite fibers.^[58–60] The elongation at break of our AG-DWCNTFs is 3.5 times higher than that of commercial PBO fiber,^[61] and 4.1 times higher than that of commercial Kevlar fiber.^[56] Therefore, our AG-DWCNTFs have great promise for applications in impact-resistant materials with high conductivity.

Good flexibility is very important for the application of next-generation lightweight conducting wires. We measured the resistance of AG-DWCNTFs during 5000 cycles of bending to an angle of 60° (Figure S21, Supporting Information). It can be seen that the change in the resistance of our AG-DWCNTFs is only 3.4%, much smaller than 8% for commercial Cu wire that had experienced identical bending. We also compared the resistance change of the AG-DWCNTF with commercial Cu wire at elevated temperatures. As shown in Figure 5e, the AG-DWCNTF has a much smaller temperature coefficient of resistance ($2.09 \times 10^{-3} \text{ K}^{-1}$) than that of commercial Cu wire ($4.10 \times 10^{-3} \text{ K}^{-1}$) in the temperature range of 293–573 K, indicating its much better temperature stability. We further measured the electrical conductivity and mechanical properties of AG-DWCNTF after the temperature stability experiment. As shown in Figure S22 (Supporting Information), the conductivity of AG-DWCNTF decreased by 11%, while the strength increased by 13%. This phenomenon originates from the de-doping of CSA in CNTFs.^[62,63]

We also demonstrated the electric heating function of our CNTFs. As shown in Figure S23a–e (Supporting Information), the temperature of our AG-DWCNTF increased rapidly to an in-

candescent state within less than 0.008 s and stabilized under a vacuum pressure of 0.1 Pa by applying 1 V voltage, which is much better than that of commercial W-Re alloy (Figure S23f–h, Supporting Information).

As discussed above, we obtained densely packed, highly aligned DWCNTFs by combining gravity withdrawing in the wet-spinning process. The achieved DWCNTFs show excellent electrical and mechanical properties. We used a multifunctional metric—the product of conductivity and tensile strength suggested by Bulmer et al.,^[64] which can easily identify materials with the highest strength and conductivity concurrently. As shown in Figure S24 (Supporting Information), the multifunctional metric (conductivity multiplied by tensile strength) of AG-DWCNTF is obviously better than that of traditional metals, which are expected to be used as suspended cables.^[64] In order to emphasize the contribution of gravity drawing, a radial plot comparing the properties of AG-DWCNTF and N-DWCNTF is shown in Figure 5f. Owing to the introduction of air gap in wet spinning, the maximum electrical conductivity, ampacity, tensile strength, and toughness of DWCNTFs reached $11.01 \pm 0.32 \text{ MS m}^{-1}$, $0.80 \pm 0.07 \text{ GA m}^{-2}$, $1.65 \pm 0.07 \text{ GPa}$ and $130.9 \pm 19.6 \text{ MJ m}^{-3}$, respectively, much higher than the corresponding values of N-DWCNTFs. The strategy of introducing an air gap to use gravity in wet spinning provides a simple way of assembling CNTFs with excellent performance.

3. Discussion

Dry-jet wet spinning is commonly recognized to provide spinning dope high shear forces to orient fibers. In this work, we tried to increase the shear rate by reducing the needle diameter and increasing the injection rate to investigate the in-depth mechanism of air gap function. As shown in Figure S25a–c (Supporting Information), it is difficult to extrude the spinning solution from a smaller needle with a diameter of 150 μm due to blockage. This result suggests that it is difficult to further increase shear force by reducing needle diameter. We further tried to increase the shear rate by increasing the injection rate. However, the collection rate needs to be correspondingly increased, which decreases the actual draw ratio. In consequence, the spinning flow cannot withstand high drawing due to the shear thinning of non-Newtonian fluid,^[65] which leads to poorly oriented and densified CNTs, and hence decreased fiber conductivity (Figure S25d, Supporting Information). Therefore, increasing the shear rate by using a thinner needle or increasing the injection rate is not valid to further improve the conductivity of CNTFs in this work. However, the introduction of a long air gap during wet spinning fully uses the function of gravity and efficiently improves the orientation and density of CNT fibers (Figure S12, Supporting Information). As a result, the electrical conductivity and tensile strength of the DWCNTFs were improved by 89.8% and 179.5% (Figure 4a), respectively.

In order to investigate the universality of dry-jet wet spinning, we also tried to spin single-wall CNT (SWCNT) fibers and few-wall CNT (FWCNT) fibers using this method. However, we found that it is difficult to form a stable air gap for FWCNTs and to form a long air gap for SWCNTs (Figure S26, Supporting Information). In consequence, the electrical conductivity and tensile strength improvement for SWCNTFs are only 19.8% and 27.8%

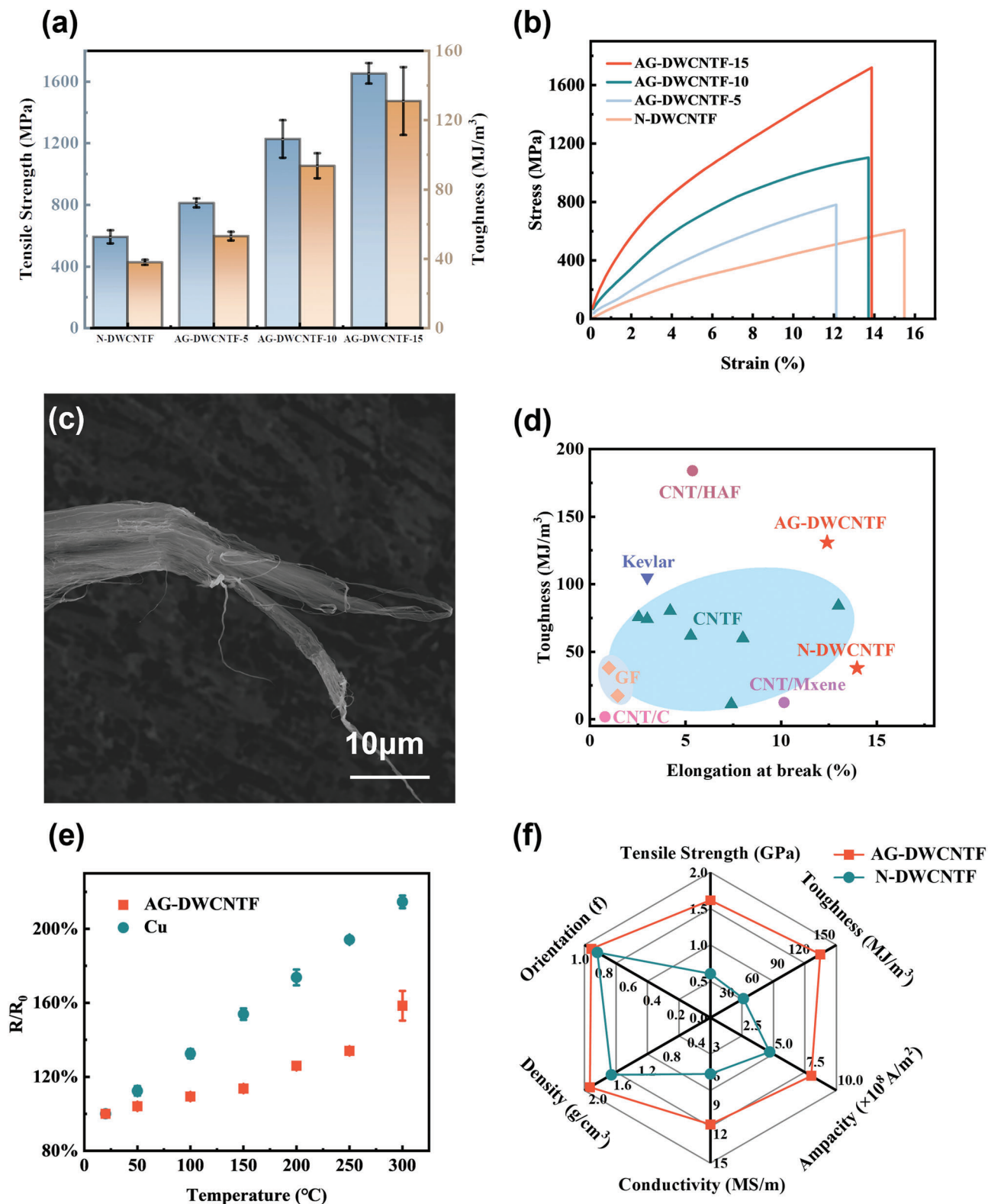


Figure 5. Comprehensive performance of DWCNTFs. a) Tensile strength and toughness of the DWCNTFs. b) The stress-strain curves of the DWCNTFs. c) SEM image of the fracture point of AG-DWCNTF. d) A comparison of elongation at break and toughness of commercial high-performance fibers, GFs and CNTFs. e) Comparison of the electrical resistance of DWCNTFs and Cu at different temperatures. f) A radar performance comparison of AG-DWCNTF and N-DWCNTF.

(Figure S27a, Supporting Information), due to the limited enhancing function of gravity in this case. We attribute this phenomenon to the difference of molecular weight and length for different CNTs. As shown in Figure S27b (Supporting Information), the DWCNTs we used have both high molecular weight and long length, which leads to a strong van der Waals force to overcome the gravity drawing to form a stable and long air gap. As a result, the orientation of the CNTs is efficiently enhanced by the gravity effect.

4. Conclusion

We have developed an efficient dry-jet wet-spinning method that combines the effect of gravity and drawing during wet spinning process to fabricate ultra-aligned, densely-packed DWCNTFs. This strategy strengthens the positive traction induced by drawing and the uniform alignment of CNTs in both the shell and core of the fiber. As a result, the DWCNTFs produced had both excellent electrical properties (conductivity of $11.01 \pm 0.32 \text{ MS m}^{-1}$ and ampacity of $0.80 \pm 0.07 \text{ GA m}^{-2}$) and mechanical properties (tensile strength of $1.65 \pm 0.07 \text{ GPa}$ and toughness of $130.9 \pm 19.6 \text{ MJ m}^{-3}$). In particular, our AG-DWCNTF had an ultrahigh specific electrical conductivity of $5.62 \times 10^3 \text{ S m}^2 \text{ kg}^{-1}$, 86% of that of Cu and exceeding most metals (Au, Mo, and Ni). Furthermore, the specific ampacity of the AG-DWCNTF reached $4.09 \times 10^5 \text{ A m kg}^{-1}$, 3 times that of commercial Cu wires, showing its great potential for use as next-generation lightweight and multifunctional conducting wires.

5. Experimental Section

Fabrication of High-Quality DWCNTs: DWCNTs were prepared by an injection FCCVD method.^[29–31] A corundum tube with a diameter of 40 mm was placed in a horizontal tube furnace as a reactor. Under the protection of a N_2 gas flow (2000 sccm), the furnace temperature was increased to 1150°C at a rate of $10^\circ\text{C min}^{-1}$. When the temperature became stable, 3000 sccm of H_2 , 30 sccm of CH_4 , and 12 sccm of C_2H_4 were introduced. A mixed solution containing toluene, ferrocene, and thiophene (Fe:S molar ratio from 16 to 5) was injected into the growth zone using a syringe pump at a rate of 1.06 mL min^{-1} . The growth time was set to be 2 h.

Fabrication of DWCNTFs: The first step was to prepare a spinnable liquid crystal solution. DWCNTs were mixed with 99% CSA (Sigma–Aldrich) to form a spinnable liquid crystalline solution using a planet mixer (Flack-Tek SpeedMixer DAC150.1 FVZ-K). The solution was then passed through a needle with an inner diameter of $180 \mu\text{m}$ at a rate of 0.10 mL min^{-1} and then flowed through the air gap (0–150 mm length) into the coagulation bath containing acetone for double diffusion during coagulation. Then the fiber flowed through an ethanol bath to remove the residual acetone. All DWCNTFs were spun at the optimal draw ratio. The collection rate was $100\text{--}230 \text{ mms}^{-1}$, which was higher than the extrusion speed to ensure fiber tension. The preparation of N-DWCNTF was to directly inject the spinning solution into the coagulation bath.

Characterization of DWCNTs and Fibers: A linear density tester^[1] (XD-1; Shanghai New Fiber Instrument Co., Ltd.) was used to measure the linear density of the fiber. Subsequently, the density of the fiber was obtained by:

$$\rho = \frac{\mu}{\pi \cdot r^2} \cdot 100 \quad (1)$$

where ρ (g cm^{-3}) is the density of fiber, μ (dtex) is the linear density of fiber, r (μm) is the radius of fiber. The diameter of each fiber was averaged by at least 30 randomly measured diameters under SEM.

Raman spectra of DWCNTs and fibers were obtained using a WITec Alpha 300R Raman spectrometer. Thermogravimetric curves of the DWCNTs were obtained using a NETZSCH STA449F5 thermal gravimetric analyzer (TGA). TEM characterization of the DWCNTs was performed using a Tecnai G2 F20 (operated at 200 kV) TEM. The diameter and surface morphology of the DWCNT fibers were characterized using a SEM (A FEI Verios G4). For cross-sectional SEM observations, the fibers were cut by a potassium ion beam with a current of 3 nA using a Zeiss Orion Nanofab equipment. The electrical resistance was measured by the four-point probe method on 5 cm-long single fibers using a Keithley 2401 Source Meter. The ampacity of the DWCNT fibers was measured using a Keithley 2460 Source Meter. To observe the cross-section morphology, DWCNTFs were cut by Thermo Scientific Scios 2 FIB and characterized using FEI Themis Z. XRM images of the DWCNTs were characterized by Xradia 800 Ultra. For the bending test, the two ends of CNTFs or Cu wires with a length of 5 cm were fixed, and the fibers/wires were shifted to the same distance to ensure a same bending angle of 60° .

Simulation of CNT Orientation: Discrete elements add fluid coupling is used to perform the simulation. In order to simplify the simulation process and reflect the changing trend of the orientation, the spinning liquid column after extrusion is simplified to be a cone.

Supporting Information

Supporting Information is available from the Wiley Online Library or from the author.

Acknowledgements

This work was supported by the National Key Research and Development Program of China (2022YFA1203302), the National Natural Science Foundation of China (Grants 52130209, 52372053, 52072375, and 52188101), the Liaoning Revitalization Talents Program (XLYC2002037), and the Basic Research Project of the Natural Science Foundation of Shandong Province, China (ZR2019ZD49).

Conflict of Interest

The authors declare no conflict of interest.

Data Availability Statement

Research data are not shared.

Keywords

ampacity, conductivity, double-wall carbon nanotube, fiber, gravity

Received: March 15, 2024

Revised: May 28, 2024

Published online: July 10, 2024

[1] L. L. Xu, X. Y. Jiao, C. Shi, H. M. Cheng, P. X. Hou, C. Liu, A. P. Wu, *ACS Nano* **2023**, 17, 9245.

[2] Z. Q. Gao, L. L. Xu, X. Y. Jiao, X. Li, C. J. He, H. Z. Wang, C. Y. Sun, P. X. Hou, C. Liu, H. M. Cheng, *ACS Nano* **2023**, 17, 18290.

[3] H. D. Bai, S. Li, J. Barreiros, Y. Q. Tu, C. R. Pollock, R. F. Shepherd, *Science* **2020**, 370, 848.

- [4] P. R. Wang, F. Q. Liu, H. Wang, H. Li, Y. Z. Gou, *J. Mater. Sci. Technol.* **2019**, *35*, 2743.
- [5] T. Z. Zhou, Y. Z. Yu, B. He, Z. Wang, T. Xiong, Z. X. Wang, Y. T. Liu, J. W. Xin, M. Qi, H. Z. Zhang, X. H. Zhou, L. H. Gao, Q. F. Cheng, L. Wei, *Nat. Commun.* **2022**, *13*, 4564.
- [6] C. Subramaniam, T. Yamada, K. Kobashi, A. Sekiguchi, D. N. Futaba, M. Yumura, K. Hata, *Nat. Commun.* **2013**, *4*, 2202.
- [7] B. Q. Wei, R. Vajtai, P. M. Ajayan, *Appl. Phys. Lett.* **2001**, *79*, 1172.
- [8] D. A. Walters, L. M. Ericson, M. J. Casavant, J. Liu, D. T. Colbert, K. A. Smith, R. E. Smalley, *Appl. Phys. Lett.* **1999**, *74*, 3803.
- [9] M. F. Yu, O. Lourie, M. J. Dyer, K. Moloni, T. F. Kelly, R. S. Ruoff, *Science* **2000**, *287*, 637.
- [10] T. W. Ebbesen, H. J. Lezec, H. Hiura, J. W. Bennett, H. F. Ghaemi, T. Thio, *Nature* **1996**, *382*, 54.
- [11] H. J. Dai, E. W. Wong, C. M. Lieber, *Science* **1996**, *272*, 523.
- [12] A. Peigney, C. Laurent, E. Flahaut, R. R. Bacsá, A. Rousset, *Carbon* **2001**, *39*, 507.
- [13] L. M. Ericson, H. Fan, H. Q. Peng, V. A. Davis, W. Zhou, J. Sulpizio, Y. H. Wang, R. Booker, J. Vavro, C. Guthy, A. N. G. Parra-Vasquez, M. J. Kim, S. Ramesh, R. K. Saini, C. Kittrell, G. Lavin, H. Schmidt, W. W. Adams, W. E. Billups, M. Pasquali, W. F. Hwang, R. H. Hauge, J. E. Fischer, R. E. Smalley, *Science* **2004**, *305*, 1447.
- [14] N. Behabtu, C. C. Young, D. E. Tsentalovich, O. Kleinerman, X. Wang, A. W. K. Ma, E. A. Bengio, R. F. ter Waarbeek, J. J. de Jong, R. E. Hoogerwerf, S. B. Fairchild, J. B. Ferguson, B. Maruyama, J. Kono, Y. Talmon, Y. Cohen, M. J. Otto, M. Pasquali, *Science* **2013**, *339*, 182.
- [15] B. Vigolo, A. Penicaud, C. Coulon, C. Sauder, R. Pailler, C. Journet, P. Bernier, P. Poulin, *Science* **2000**, *290*, 1331.
- [16] K. L. Jiang, Q. Q. Li, S. S. Fan, *Nature* **2002**, *419*, 801.
- [17] K. Koziol, J. Vilatela, A. Moissala, M. Motta, P. Cuniff, M. Sennett, A. Windle, *Science* **2007**, *318*, 1892.
- [18] S. G. Kim, G. M. Choi, H. D. Jeong, D. Lee, S. Kim, K. H. Ryu, S. Lee, J. Kim, J. Y. Hwang, N. D. Kim, D. Y. Kim, H. S. Lee, B. C. Ku, *Carbon* **2022**, *196*, 59.
- [19] D. E. Tsentalovich, R. J. Headrick, F. Mirri, J. L. Hao, N. Behabtu, C. C. Young, M. Pasquali, *ACS Appl. Mater. Interfaces* **2017**, *9*, 36189.
- [20] L. W. Taylor, O. S. Dewey, R. J. Headrick, N. Komatsu, N. M. Peraca, G. Wehmeyer, J. Kono, M. Pasquali, *Carbon* **2021**, *171*, 689.
- [21] M. B. Jakubinek, M. B. Johnson, M. A. White, C. Jayasinghe, G. Li, W. D. Cho, M. J. Schulz, V. Shanov, *Carbon* **2012**, *50*, 244.
- [22] M. H. Miao, *Carbon* **2011**, *49*, 3755.
- [23] W. B. Lu, M. Zu, J. H. Byun, B. S. Kim, T. W. Chou, *Adv. Mater.* **2012**, *24*, 1805.
- [24] F. M. Guo, C. Li, J. Q. Wei, R. Q. Xu, Z. L. Zhang, X. Cui, K. L. Wang, D. H. Wu, *Mater. Res. Express* **2015**, *2*, 095604.
- [25] T.-S. Chung, X. Hu, *J. Appl. Polym. Sci.* **1997**, *66*, 1067.
- [26] W. Fang, E. Y. Lim, K. L. Nieminen, H. Sixta, *ACS Omega* **2023**, *8*, 34103.
- [27] J. Liang, Q. Xie, W. Feng, B. Li, T. Peng, K. Liu, M. Jiang, *Fibers Polym.* **2023**, *24*, 3861.
- [28] M. J. Lundahl, V. Klar, R. Ajdary, N. Norberg, M. Ago, A. G. Cunha, O. J. Rojas, *ACS Appl. Mater. Interfaces* **2018**, *10*, 27287.
- [29] P. X. Hou, B. Yu, Y. Su, C. Shi, L. L. Zhang, C. Liu, S. S. Li, J. H. Du, H. M. Cheng, *J. Mater. Chem. A* **2014**, *2*, 1159.
- [30] J. Q. Wei, L. J. Ci, B. Jiang, Y. H. Li, X. F. Zhang, H. W. Zhu, C. L. Xu, D. H. Wu, *J. Mater. Chem.* **2003**, *13*, 1340.
- [31] Z. P. Wu, Q. F. Xu, J. N. Wang, J. Ma, *J. Mater. Sci. Technol.* **2010**, *26*, 20.
- [32] V. A. Davis, A. N. G. Parra-Vasquez, M. J. Green, P. K. Rai, N. Behabtu, V. Prieto, R. D. Booker, J. Schmidt, E. Kesselman, W. Zhou, H. Fan, W. W. Adams, R. H. Hauge, J. E. Fischer, Y. Cohen, Y. Talmon, R. E. Smalley, M. Pasquali, *Nat. Nanotechnol.* **2009**, *4*, 830.
- [33] N. Behabtu, M. J. Green, M. Pasquali, *Nano Today* **2008**, *3*, 24.
- [34] C. Hou, R.-j. Qu, Y. Liang, C.-g. Wang, *J. Appl. Polym. Sci.* **2005**, *96*, 1529.
- [35] D. R. Paul, *J. Appl. Polym. Sci.* **1968**, *12*, 383.
- [36] J. Chen, C. G. Wang, X. G. Dong, H. Z. Liu, *J. Polym. Res.* **2006**, *13*, 515.
- [37] J. Luo, Y. Wen, X. Jia, X. Lei, Z. Gao, M. Jian, Z. Xiao, L. Li, J. Zhang, T. Li, H. Dong, X. Wu, E. Gao, K. Jiao, J. Zhang, *Nat. Commun.* **2023**, *14*, 3019.
- [38] S. J. Wan, Y. Chen, S. L. Fang, S. J. Wang, Z. P. Xu, L. Jiang, R. H. Baughman, Q. F. Cheng, *Nat. Mater.* **2021**, *20*, 624.
- [39] P. Li, Y. J. Liu, S. Y. Shi, Z. Xu, W. G. Ma, Z. Q. Wang, S. P. Liu, C. Gao, *Adv. Funct. Mater.* **2020**, *30*, 2006584.
- [40] H. D. Jeong, S. G. Kim, G. M. Choi, M. Park, B. C. Ku, H. S. Lee, *Chem. Eng. J.* **2021**, *412*, 128650.
- [41] X. Wang, N. Behabtu, C. C. Young, D. E. Tsentalovich, M. Pasquali, J. Kono, *Adv. Funct. Mater.* **2014**, *24*, 3241.
- [42] Y. X. Bai, M. Q. Zhu, S. J. Wang, L. Q. Liu, Z. Zhang, *Carbon* **2023**, *202*, 425.
- [43] X. Y. Jiao, C. Shi, Y. M. Zhao, L. L. Xu, S. K. Liu, P. X. Hou, C. Liu, H. M. Cheng, *ACS Nano* **2022**, *16*, 20263.
- [44] B. S. Han, E. Y. Guo, X. Xue, Z. Y. Zhao, L. S. Luo, H. T. Qu, T. Niu, Y. J. Xu, H. L. Hou, *Carbon* **2017**, *123*, 593.
- [45] H. B. Lee, S. H. Noh, T. H. Han, *Chem. Eng. J.* **2021**, *414*, 128803.
- [46] J. Y. Zou, D. D. Liu, J. N. Zhao, L. G. Hou, T. Liu, X. H. Zhang, Y. H. Zhao, Y. T. T. Zhu, Q. W. Li, *ACS Appl. Mater. Interfaces* **2018**, *10*, 8197.
- [47] F. Daneshvar, H. X. Chen, T. Zhang, H. J. Sue, *Adv. Mater. Interfaces* **2020**, *7*, 2000779.
- [48] A. Lekawa-Raus, J. Patmore, L. Kurzepa, J. Bulmer, K. Koziol, *Adv. Funct. Mater.* **2014**, *24*, 3661.
- [49] P. C. Collins, M. S. Arnold, P. Avouris, *Science* **2001**, *292*, 706.
- [50] J. J. Vilatela, J. A. Elliott, A. H. Windle, *ACS Nano* **2011**, *5*, 1921.
- [51] Y. N. Zhang, L. X. Zheng, G. Z. Sun, Z. Y. Zhan, K. Liao, *Carbon* **2012**, *50*, 2887.
- [52] M. Zhang, K. R. Atkinson, R. H. Baughman, *Science* **2004**, *306*, 1358.
- [53] X. F. Zhang, Q. W. Li, T. G. Holesinger, P. N. Arendt, J. Y. Huang, P. D. Kirven, T. G. Clapp, R. F. DePaula, X. Z. Liao, Y. H. Zhao, L. X. Zheng, D. E. Peterson, Y. T. Zhu, *Adv. Mater.* **2007**, *19*, 4198.
- [54] M. Motta, Y. L. Li, I. Kinloch, A. Windle, *Nano Lett.* **2005**, *5*, 1529.
- [55] M. Motta, A. Moissala, I. A. Kinloch, A. H. Windle, *Adv. Mater.* **2007**, *19*, 3721.
- [56] I. O'Connor, H. Hayden, J. N. Coleman, Y. K. Gun'ko, *Small* **2009**, *5*, 466.
- [57] G. Q. Xin, T. K. Yao, H. T. Sun, S. M. Scott, D. L. Shao, G. K. Wang, J. Lian, *Science* **2015**, *349*, 1083.
- [58] J. M. Razal, J. N. Coleman, E. Munoz, B. Lund, Y. Gogotsi, H. Ye, S. Collins, A. B. Dalton, R. H. Baughman, *Adv. Funct. Mater.* **2007**, *17*, 2918.
- [59] X. Zhao, J. Z. Zhang, K. Lv, N. Kong, Y. Q. Shao, J. L. Tao, *Carbon* **2022**, *200*, 38.
- [60] H. Mei, Q. L. Bai, T. M. Ji, H. Q. Li, L. F. Cheng, *Compos. Sci. Technol.* **2014**, *103*, 94.
- [61] S. Kumar, T. D. Dang, F. E. Arnold, A. R. Bhattacharyya, B. G. Min, X. Zhang, R. A. Vaia, C. Park, W. W. Adams, R. H. Hauge, R. E. Smalley, S. Ramesh, P. A. Willis, *Macromolecules* **2002**, *35*, 9039.
- [62] D. Lee, S. G. Kim, S. Hong, C. Madrona, Y. Oh, M. Park, N. Komatsu, L. W. Taylor, B. Chung, J. Kim, J. Y. Hwang, J. Yu, D. S. Lee, H. S. Jeong, N. H. You, N. D. Kim, D. Y. Kim, H. S. Lee, K. H. Lee, J. Kono, G. Wehmeyer, M. Pasquali, J. J. Vilatela, S. Ryu, B. C. Ku, *Sci. Adv.* **2022**, *8*, eabn0939.

- [63] X. Zhang, M. De Volder, W. B. Zhou, L. Issman, X. J. Wei, A. Kaniyoor, J. T. Portas, F. Smail, Z. B. Wang, Y. C. Wang, H. P. Liu, W. Y. Zhou, J. Elliott, S. S. Xie, A. Boies, *Sci. Adv.* **2022**, *8*, eabq3515.
- [64] J. S. Bulmer, A. Kaniyoor, J. A. Elliott, *Adv. Mater.* **2021**, *33*, 46.
- [65] F. Mirri, N. D. Orloff, A. M. Forster, R. Ashkar, R. J. Headrick, E. A. Bengio, C. J. Long, A. Choi, Y. Luo, A. R. Hight Walker, P. Butler, K. B. Migler, M. Pasquali, *ACS Appl. Mater. Interfaces* **2016**, *8*, 4903.